



3

4

5

7 8

9

10

11

12

13

14

15

16

17

18

19

20

21

22

23

24

25

26

27

28

29

31

32

33

34

35

36

37

38

39

40

41

42

43

Article

# Monitoring epoxy coated steel under combined mechanical loads and corrosion using fiber Bragg grating sensors

Luyang Xu<sup>1</sup>, Dawei Zhang<sup>1</sup>, Ying Huang<sup>1\*</sup>, Shuomang Shi<sup>1</sup>, Hong Pan<sup>1</sup>, and Yi Bao<sup>2</sup>

- Department of Civil, Construction, and Environmental Engineering, North Dakota State University, Fargo 58102
- <sup>2</sup> Department of Civil, Environmental and Ocean Engineering, Stevens Institute of Technology, Hoboken, New Jersey 07030
- \* Corresponding authors: ving.huang@ndsu.edu

Abstract: Fiber Bragg grating (FBG) sensors have been applied to assess strains, stresses, loads, corrosion, and temperature for structural health monitoring (SHM) of steel infrastructure such as buildings, bridges, and pipelines. Since a single FBG sensor measures a particular parameter at a local spot, it is challenging to detect different types of anomalies and interactions of anomalies. This paper presents an approach to assess interactive anomalies caused by mechanical loading and corrosion on epoxy coated steel substrates using FBG sensors in real time. Experiments were performed by comparing the monitored center wavelength changes in the conditions with loading only, corrosion only, and simultaneous loading and corrosion. The theoretical and experimental results indicated that there were significant interactive influences between loading and corrosion for steel substrates. Loading accelerated the progress of corrosion for the epoxy coated steel substrate, especially when delamination in epoxy coating was noticed. Through the real-time monitoring from the FBG sensors, the interactions between the anomalies induced by the loading and corrosion can be quantitatively evaluated through the corrosion depth and the loading contact length. These fundamental understanding on the interactions of different anomalies on the steel structures can provide valuable information to the engineers for better management of steel structures.

**Keywords:** Corrosion; fiber Bragg grating (FBG) sensors; interactive anomalies; structural health monitoring (SHM)

Citation: Lastname, F.; Lastname, F.; Lastname, F. Title. Sensors 2022, 22, x. https://doi.org/10.3390/xxxxx

Academic Editor: Firstname Lastname

Received: date Accepted: date Published: date

**Publisher's Note:** MDPI stays neutral with regard to jurisdictional claims in published maps and institutional affiliations.



Copyright: © 2022 by the authors. Submitted for possible open access publication under the terms and conditions of the Creative Commons Attribution (CC BY) license (https://creativecommons.org/licenses/by/4.0/).

1. Introduction

Reinforced concrete (RC) and steel are the most common construction materials for civil infrastructures [1,2]. As time goes, civil infrastructures made by reinforced concrete or steel will deteriorate and anomalies or damages may accumulate in the structures, which may result in safety concerns of structures that lead to tragedies of property and life losses. Among various types of structural degradations, steel corrosion and local stress accumulations are well known as several of those main concerns/threats to the structural integrity, durability and reliability of RC and steel structures. To prevent and mitigate steel corrosion, various protective measures can be applied to steel in the RC or steel structures such as cathodic protection, corrosion inhibitor, anti-corrosion alloys and coatings. Cathodic protection mitigates corrosion through the use of the metal as the cathode of an electrochemical cell [3, 4]. Corrosion inhibitor prevents access of the corrosive substance to the metal, thus, prevents corrosion [5, 6]. The anti-corrosion alloys forms corrosionresistant alloys like stainless steel alloys, aluminum alloys through adding high corrosionresistant components into the steel materials [7]. Compared to the above-mentioned corrosion mitigation approaches, the application of anti-corrosive coatings is a cost-effective method to protect metals with additional benefit to reduce local stress accumulations since they provide an extra layer between the substrates and loading [8, 9]. Among the

anti-corrosive coatings, a thin layer of epoxy coating is one of the most commonly coatings to isolate structures from the external corrosive environment for steel corrosion protection [10-12].

In addition to protective coatings, to detect steel corrosion and loading induced damages, in practice, visual inspection is commonly applied due to its simplicity. However, the visual inspection may not be accurate as the occurrence of corrosion or loading induced damages usually are located beneath the protective coatings and hard to be seen directly, and it may not be timely due to the large scale of the associated structures [13]. Searching for a more reliable inspection method for steel corrosion, weight loss coupon measurement is widely used in practice, in which steel coupons are placed at the location of concerns and weight losses are measured after a period time of exposure to estimate corrosion rates [14]. This approach is more quantitively compared to visual inspection, however, it suffers from some unavoidable drawbacks, such as long inspection time, high maintenance, and labor costs. Additionally, this method cannot detect loading induced damages on the structure and also may need to disassemble a part of structures resulting in loss of structural integrity.

To address the limitations of the above-mentioned traditional approaches to detect steel corrosion and local stress accumulations, non-destructive evaluation (NDE) methods become popular. The NDE methods do not bring any interruptions or damages to the original structures as well as bringing in high accuracy and ease of use. However, most NDE techniques are highly dependent on the applied sensors that mostly rely on the transmission and detection of electrical signals such as acoustic and ultrasonic sensors, magnetic sensors, microwave, or guided wave sensors, etc., resulting in lack of detection accuracy with the existence of electrical-magnetic interference in the field applications [15, 16]. More importantly, as the NDE techniques are mostly external to a structure, its application may require additional tool sets and skilled labors. Therefore, the NDE techniques are usually used for scheduled periodic inspections or inspection in needs and may not be cost effective for the wide and long-term monitoring applications [2].

In recent years, structural health monitoring (SHM) has been widely recognized as an effective onsite monitoring method of early abnormalities in many industries, such as aerospace, mechanical, and civil engineering fields [17,18]. A proper SHM system can detect early initiation of degradations and monitor the cumulation of degradations and damages such as overstress, cracks, and corrosion, in existing and new structures to guide a cost-effective structural maintenance plan and avoid collapses and the resulted tragedies [19,20]. There are many types of sensors can be used in a SHM system, such as electrical strain gauges, acoustic and ultrasonic sensors, cameras, and fiber optic sensors [21-23]. Among various existing sensors for SHM systems, fiber optic sensors, especially, fiber Bragg grating (FBG) sensors, attract intensive attentions from researchers due to the unique advantages of high sensitivity and precision, satisfiable linearity, immunity to electromagnetic interference, resistance to harsh environments, lightweight, small physical dimensions, easy-operability, and relatively low cost [2,24]. The FBG sensors, as the most commonly used fiber optic sensors, have been applied in many industries for monitoring of strains, stress, loads, and temperatures [17]. As corrosion can be investigated by monitoring the strain changes inside or on the surface of a steel structural component, FBG sensors have been also applied to detect steel corrosion for bare and coated steel structures [25-27].

Although the FBG sensors have been used as a tool to monitor the structural performance and damages, as an FBG sensor belongs to a category of local point sensors, most of the research used FBG sensors to detect one single measure of structural performance or damage. However, structures may not only suffer from corrosion, but also have damages induced by accumulation of local stresses as various natural factors such as wind, snow, and moving loads may introduce extreme loads to structures.

Recent investigations have shown that the interaction of loading and corrosion could mutually promote damages induced by each other, which may pose threats to the health

condition and safety of structures. Accelerated corrosion results from previous research [28] indicated that the compressive load level could simultaneously influence the corrosion rate of steel bar and the corrosive cracking behavior of reinforced concrete. Through the evaluation of the deflections of RC beams under load and accelerated corrosion, it was noticed that during the initial stage of corrosion, the deflections of beams increased significantly due to the flexural tension and the expansive stresses caused by corrosion products, resulting in crack propagations on the tension sides of beams [29]. In addition, researchers found out that both the corrosion of reinforcements and the cyclic loading obviously reduced the bond properties of concrete structures [30]. Severe corrosion led to significant degradation of the bond during the first five cycles, corrosion process was weakened with loading, and the corrosion of rebars under compression was more severe than that under tension [31].

However, to date, there is yet real-time monitoring of the interaction between corrosion and load induced damages on steel structures. In this paper, systematic experimental studies were performed to investigate such interactive influences between steel corrosion and static loads on epoxy coated steel using FBG sensors. Periodic temporary static loads were applied every six days on the coated steel substrates which were immersed in 3.5% NaCl solutions for accelerated corrosion. The interactions between the loads and corrosion were investigated by data mining the patterns of the recorded center wavelength changes of the FBG sensors.

# 2. Theoretic Analysis

## 2.1. Sensing principles

A typical single-mode optical fiber is composed of fused silica core and cladding. An FBG sensor is manufactured by engraving periodic Bragg gratings in an optical fiber. When the incident light passes through the gratings, light waves with a specific Bragg wavelength ( $\lambda_B$ ) is reflected, while the rest of light waves is transmitted. The value of Bragg wavelength ( $\lambda_B$ ) of a FBG sensor can be determined using the effective refractive index ( $n_{eff}$ ) of the fiber and the Bragg grating period ( $\Lambda$ ) [24, 33, 34]as:

$$\lambda_B = 2n_{eff} \cdot \Lambda \tag{1}$$

The effective refractive index of a particular FBG sensor is a constant, while the fiber Bragg grating period is sensitive to temperature and strain changes [35]:

$$\Delta \lambda = \lambda_B [(1 - P_e) \cdot \varepsilon_c + (\alpha + \xi) \Delta T]$$
 (2)

where  $\Delta\lambda$  is the Bragg wavelength shift;  $P_e$  is the photo elastic coefficient of the fiber;  $\varepsilon_c$  is the strain change along the grating direction;  $\alpha$  and  $\xi$  are the thermo expansion coefficient and the thermo-optic coefficient of the fiber, respectively; and  $\Delta T$  is the change of external temperature. If the temperature is unchanged or compensated using a FBG sensor that is nearby and free of strain change, Eq. (2) can be rewritten as:

$$\Delta \lambda = \lambda_B (1 - P_e) \cdot \varepsilon_c \tag{3}$$

Strain changes along the grating can be determined by measuring the wavelength shift of a FBG sensor. The strain changes can be induced by mechanical loads, corrosion, and other effects.

#### 2.2. Calibration of FBG sensors

In this study, the FBG sensors were attached to steel specimens using a two-part epoxy. The epoxy served as adhesive and provided protection for the optical fiber. The strain sensitivity of the FBG sensor embedded in epoxy was calibrated through tension tests to eliminate the strain transfer effect [36-38] on the strain measurement results. The strain transfer ratio (k) is expressed as [39]:

$$k = \frac{\varepsilon_c}{\varepsilon_1} \tag{4}$$

where  $\varepsilon_1$  is the strain in the steel plate, and  $\varepsilon_c$  is the strain measured from the FBG sensor.

The test was performed using an MTS loading machine under tension as shown in Fig. 1(a). The strain in the steel plate was evaluated using an extensometer, and the strain in the FBG sensor was simultaneously measured using an interrogator (model: National Instrument NI PXIe-1071) as shown in Fig. 1(b). The sampling rate of the interrogator and MST machine were 10 Hz.





(a) (b)

Fig. 1 Calibration of strain transfer ratio: (a) tensile test setup, and (b) FBG interrogator.

Fig. 2 shows the tensile test data. The strains in the steel plate and the FBG sensor were approximately proportional. The slope of the curve represents the strain transfer ratio, which is 0.39 according to linear regression. The coefficient of determination of the linear regression analysis was 0.99.

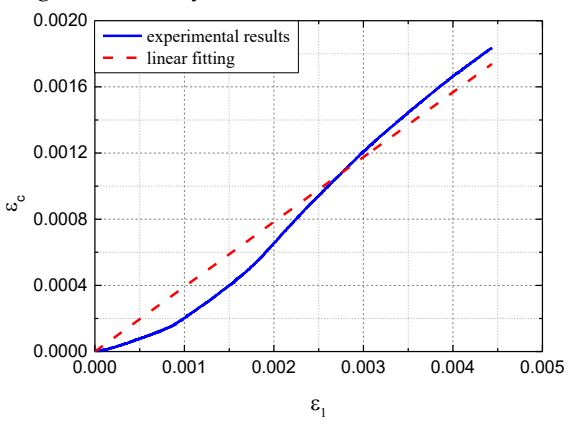


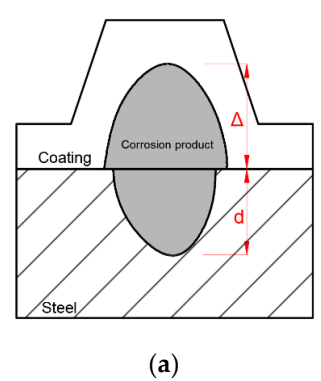
Fig. 2 Calibration results of the strain transfer ratio of the adopted FBG sensors.

## 2.3. Measuring the depth of pitted corrosion

Corrosion of a local spot where the protective coating of steel is damaged is categorized as pitted corrosion. Previous studies [40-46] assumed that the corrosion products of pitted corrosion mainly accumulate within a small area in the vertical direction. The shape of pitted corrosion is considered as the hemispherical hole, as shown in Fig. 3(a). The depth of pitted corrosion (d) can be used to characterize the severity of corrosion [47]:

$$d = \frac{1.2\Delta}{(c-1)} \tag{5}$$

where  $\Delta$  is the upward displacement of coating induced by pitted corrosion, and c is the volume ratio between the corrosion product and the original steel [47].



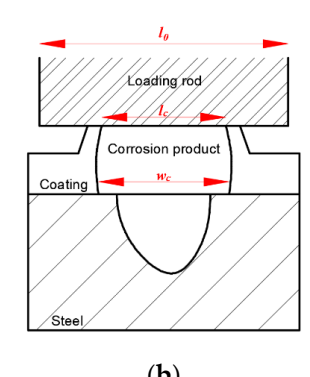


Fig. 3 Schematic illustration of pitted corrosion effect on the deformation of the epoxy coating (a) deformation under only corrosion, and (b) deformation under loading and corrosion.

If a mechanical load is applied to the location where corrosion occurs, the epoxy on top of the corrosion will be subjected to two types of forces, with one caused by the mechanical load and the other one induced by the expansion from the corrosion products, which can be simplified as concentrated loads ( $F_1$ ) and ( $F_c$ ) as shown in Fig. 4(a), respectively. As the corrosion products lift up a small area of epoxy, debonding of epoxy coating would occur along the width of the corrosion. Since all other areas other than the corrosion width remain bonded to the substrate [47], the debonded epoxy can be simplified as a fixed beam, which is subjected to both uplifting force induced by corrosion products ( $F_c$ ) and downward external mechanical load ( $F_1$ ) as shown in Fig. 4(a). In other words, the FBG sensor measures the strains in the epoxy that is subjected to a combination of mechanical loads and corrosion effect.

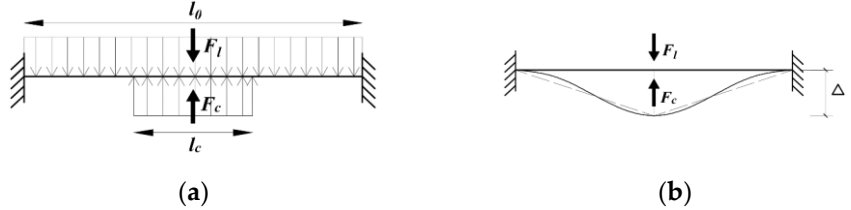


Fig. 4. Illustration of the beam model used to mimic the combined effect of corrosion and external load on the epoxy instrumented with a FBG sensor: (a) illustration of the beam model, and (b) illustration of the deformation.

In practical application of steel structures, comparing the large span of steel components, the deformation induced from external loads or corrosion is considered small. Thus, the dimension along steel surfaces generally remains curveless, from which it is assumed that in the deformation of the epoxy with FBG sensor under mechanical loading and corrosion can be simplified to be a triangular shape as shown in Fig. 4(b). When there is only external load, it can be assumed that the original length of the fixed beam model,  $L_0$ , is the diameter of the external load. The displacement at the middle span is expressed as:

$$\Delta = \frac{1}{2} \sqrt{L^2 - L_0^2} \tag{6}$$

where  $L_0$  is the original length of the beam model, and L is the deformed length of the beam model.

The strains in the embedded FBG sensor is expressed as:

$$\frac{L - L_0}{L_0} = \varepsilon_c \tag{7}$$

Substituting Eq. (7) into Eq. (6), the maximum deformation of the epoxy can be expressed as:

$$\Delta = \frac{1}{2} L_0 \cdot \sqrt{\varepsilon_c \cdot (\varepsilon_c + 2)} \tag{8}$$

With Eq. (3), (5), and (8), the depth of pitted corrosion (d) can be determined based on the wavelength shift of the FBG sensor:

$$d = \frac{0.6L_0}{(c-1)} \cdot \sqrt{\alpha \Delta \lambda \cdot (\alpha \Delta \lambda + 2)}$$
 (9)

where 
$$\alpha = \frac{1}{\lambda_B(1-P_e)}$$
.

## 2.4. Measuring the width of pitted corrosion

With the progress of corrosion and the vertical accumulation of pitted corrosion products, the FBG sensor is gradually lifted. Meanwhile, with the external load on top of the corrosion products, the debonded length of the epoxy coating, which is defined as the width of pitted corrosion,  $w_c$ , continuously changes. Before extensive corrosion and under the vertical external load, the corrosion product is compacted into a thin film. Thus, the contact length of the external load and epoxy coating,  $L_0$ , can be considered equal to the initial debonded length,  $w_c$ , as shown in Fig. 3(b). As seen in Fig. 3(b), a larger width of pitted corrosion indicates a larger corrosion product diffusion area and a larger corrosion area. Thus, the width of pitted corrosion can be used to evaluate the corrosion severity and the interaction between external load and corrosion. Based on the fixed end beam model, the maximum deflection of the beam can be more accurately estimated as:

$$\Delta = \frac{Fw_c^3}{384EI} \tag{10}$$

where  $F = F_l - F_c$ , E is the elastic modulus, and I is the moment of inertia.

Integrating Eq. (10) and Eq. (3) into Eq. (8), the relationship between the Bragg wavelength change and the loading contact length is expressed as:

$$\frac{1}{2}L_0 \cdot \sqrt{\alpha \Delta \lambda \cdot (\alpha \Delta \lambda + 2)} = \frac{Fw_c^3}{384EI} \tag{11}$$

where  $\alpha = \frac{1}{\lambda_B(1-P_e)}$ . Based on the loading only condition, by monitoring the Bragg wavelength changes under different conditions, the corresponding width of corrosion,  $w_c$  can be obtained:

$$\frac{w_c^3}{L_0^3} = \frac{\sqrt{\alpha\Delta\lambda \cdot (\alpha\Delta\lambda + 2)}}{\sqrt{\alpha\Delta\lambda_0 \cdot (\alpha\Delta\lambda_l + 2)}}$$
(12)

where  $\Delta\lambda_0$  is the Bragg wavelength change under the loading only. If  $F_1\gg F_c$ , it can be assumed that  $F=F_l-F_c\approx F_l$ . So, the width of the corrosion can be approximated as:

$$w_c = \sqrt[6]{\frac{\Delta\lambda \cdot (\alpha\Delta\lambda + 2)}{\Delta\lambda_l \cdot (\alpha\Delta\lambda_l + 2)}} \cdot L_0. \tag{13}$$

Therefore, by monitoring the Bragg wavelength changes, both the corrosion depth (d) and the width  $(w_c)$  can be measured to investigate the interaction between damages induced by external temporary loading and corrosion.

### 3. Experimental Program

To test the interaction between steel corrosion and static loads induced damages, corrosion and periodic static loads need to be applied simultaneously. However, before applying simultaneous corrosion and loads, separate loading and corrosion tests are also needed to understand how the coated steel behave under each of the conditions. Thus, one control test of loading only, and one control test of corrosion only was first conducted to compare with multiple tests with simultaneous loading and corrosion to investigate the interaction of loading and corrosion.

#### 3.1. Materials and dimensions

In all the experiments, epoxy coated steel plates were used as testing substrate. FBG sensors were embedded inside the epoxy coating at the central axis of the steel plate as shown in Fig. 5. A36 structural steel was used as the material of steel plates and their dimensions were 6.75 in.  $\times$  6.75 in.  $\times$  0.125 in . Epoxy resin (Duralco 4461) was used as the protective coating. The FBG sensors (os1100) manufactured by LUNA were used and the properties of the used FBG sensors are listed in Table 1 (provided by manufacture). The same FBG interrogator as in Fig. 1(b) was used to collect the Bragg wavelength changes.

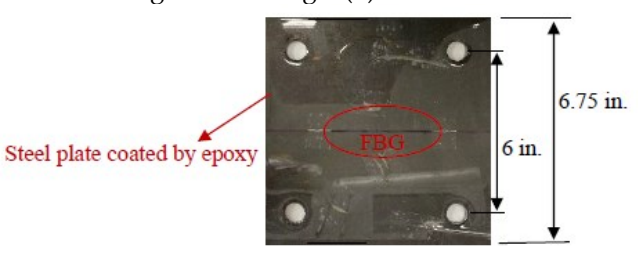


Fig. 5 An example embedded FBG sensor.

Table 1 Properties of the FBG sensors.

FBG length	10 mm
Strain limit	5,000 με
Strain sensitivity	~ 1.2 pm/με
Operating temperature range	-40 to 120 °C
Fiber coating	Polyimide
Fiber re-coating diameter	145 – 165 μm

## 3.2. Loading-only tests

# 3.2.1. Test set-up

In this paper, concentrated load was applied on top of the embedded FBG sensor to investigate the loading effects. To create a loading mechanics, the steel plate was elevated away from a perforated stainless-steel table using four stainless-steel bolts and nuts (diameter of  $\frac{1}{2}$  in.) as shown in Figs. 6(a, b). The distance between the center of two bolts was set to be 6 in. as seen in Fig. 4. Then the concentrated loads were applied at the center of the steel plate through a simple point load frame as shown in Figs. 6(a, b). A stainless-steel bar with a diameter of 0.75 in. was welded to a stainless-steel plate with a size of 6 in. × 6 in. × 0.125 in. to provide the point contact between the loads and the coated testing steel plate samples. Discrete accumulated weights were placed on top of the stainless-steel plate to generate the static loads. To be statistically valid, three identical specimens were tested in the loading-only tests in addition to a fourth specimen for temperature compensation. The samples for loading-only tests were labeled as L1, L2, L3 for loading tests and LT for temperature compensation.

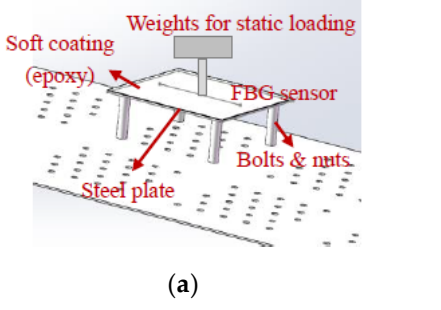




Fig. 6 Test set-up of loading experiment: (a) schematic view, and (b) a photo.

3.2.2. Determination of the static loading levels

To actually determine the loading levels to be applied on the loading frame as shown in Fig. 6(b) for inducing noticeable stress or damages on the epoxy coated steel plate, a calibration test was conducted to set up relationship between the strains on the FBG sensor and the static loads on top of the steel plate. Fig. 7 shows the test setup. The same test sample as shown in Fig. 6 was used to perform the calibration test. Instead of using discrete loads, an MTS loading machine was used to apply a gradually increase compression load on top of a  $^{3}4$  in. diameter steel rod. During the calibration test, the same sampling rate of 10 Hz was used for both the FBG interrogator and MTS machine. Fig. 8 shows the result of compression test, indicating that a linear correlation between the obtained strains ( $\mu\epsilon$ ) from the FBG sensor and the load (N).



Fig. 7 Compression test setup.

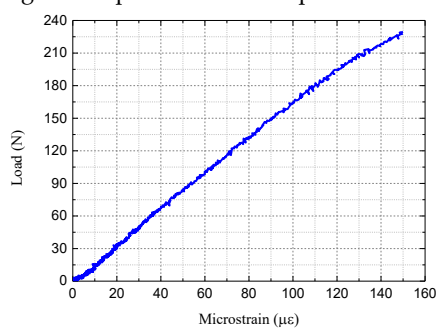


Fig. 8 Results from the loading calibration test.

Since corrosion on epoxy coated steel is a very slow process, corrosion is unlikely to induce sudden shifts of Bragg wavelength for the FBG sensors. On the other hand, loading on the FBG sensors will induce sudden significant amount of Bragg wavelength shifts. To have noticeable changes in the Bragg wavelength changes induced by loading during the further combined loading-corrosion tests, a 20 pm of Bragg wavelength change induced by a discrete load level was selected to have a more obvious observation. According to Eq. (3), a Bragg wavelength shift of 20pm is corresponding to a strain level of approximately 20  $\mu\epsilon$  in the axial direction of the FBG sensor. From Fig. 8, it can be seen that a 20  $\mu\epsilon$  of strain changes in the axial direction of the FBG sensor required a load increase of 30 N. Therefore, the discrete weight level to be placed on top of the steel plate was selected to be 30 N.

To investigate the impacts of loads on steel corrosion, a five-level loading and unloading test was designed using each load level of 30 N. To produce such a static load level, two steel plates with the size of 6 in.  $\times$  6 in.  $\times$  6 in. were fabricated and used as weight for 30N, as shown in Fig. 5(b). Thus, for the five-level loading and unloading tests, a total of 10 such steel plates were prepared. For each static weight level, a load duration of 2 min was used to ensure a stable load. Table 2 lists the static load values (N) and the corresponding theoretical expected strain levels ( $\mu \varepsilon$ ) of the five-level loading test.

Table 2 Load values and corresponding theoretical strain levels of the five-level loading test.

Load level	Load value (N)	Expected strain value ( $\mu \varepsilon$ )
1 <sup>st</sup>	30	20
$2^{\rm nd}$	60	40
3 <sup>rd</sup>	90	60

4 <sup>th</sup>	120	80
$5^{ m th}$	150	100

## 3.3. Corrosion-only tests

Corrosion-only tests were also set up to investigate how the epoxy coated steel behave under the corrosion only environments. To create a corrosion environment on the epoxy coated steel plates, PVC pipes with a diameter of 4 in. were attached on the surfaces of epoxy coated steel plate specimens using epoxy adhesive as shown in Fig. 9(a). After the adhesive was fully cured, PVC pipes were filled with 3.5wt% NaCl solution to simulate an accelerate corrosive environment. To be statistically valid, four identical specimens were tested at the same time, one of which was used for temperature compensation without loading and corrosion. The samples for corrosion-only tests were labeled as C1, C2, C3 and CT (CT was used for temperature compensation). Since epoxy coating has great corrosion protection if no defects or damages on the epoxy coatings [48], it would take too long for the corrosion tests if no pre-fabricated damages on the epoxy coating. Thus, to accelerate the corrosion process, one artificial crack with a length of 1 in. was introduced to the epoxy coating using a micro-grinder. The artificial crack was located 0.5 in. away from the FBG sensor on each steel plate sample as shown in Fig 9(b). In this paper, the corrosion tests were conducted for up to 120 days.



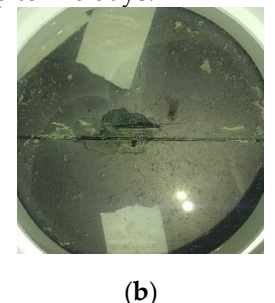
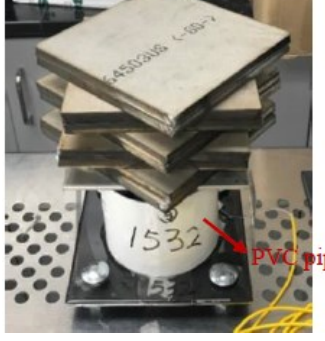


Fig. 9 Experimental setup for corrosion-only tests: (a) corrosion-only test setup, and (b) introducing artifical cracks on epoxy coating for accelerated localized corrosion.

## 3.4. Combined loading-corrosion tests

To investigate the interaction between load and corrosion induced damages, combined loading-corrosion tests were also conducted. Fig. 10 shows the designed test setup for the combined loading-corrosion tests. The corrosion test was firstly set up following the same setup as in Section 3.3. During the corrosion process, there was one cycle of static loading applied to the samples every six days following the loading test setup as in Section 3.2. Thus, during the 120 days of corrosion testing, there were 20 cycles of interactive loading tests performed on each test sample. Table 3 provides the schedule of interactive loading & corrosion tests. The same samples which previously performed loading tests, L1, L2, and L3 were used to conduct the combined loading-corrosion tests renamed B1, B2, and B3. With temperature compensation samples for each test, all the experimental results and analysis in next section are presented after compensating temperature effects.



ipe for accelerated corrosion

Fig. 10 Experimental setup for combined loading-corrosion tests

Table 3 Schedule of interactive loading & corrosion tests

Time (days)	Test Operation	
0	Corrosion test start	
4	1st cycle of loading test	
10	2nd cycle of loading test	
16	3rd cycle of loading test	
22	4th cycle loading test	
•••		
120	20th cycle of loading test	
120	Corrosion test end	

### 4. Experimental Results

### 4.1. Loading-only tests

Fig. 11 shows the Bragg wavelength shifts of three testing samples during the five-level loading and unloading tests. As each test sample were tested three times, Fig. 11 shows the average wavelength shifts for each sample. From the figure, it is noted that the wavelength changes of all three samples yielded stepwise wavelength changes. The total wavelength shifts of L1, L2 and L3 exceeded 100 pm and reached the expected wavelength variation ranges as expected in Table 1, with 180 pm, 210 pm and 110 pm, respectively. The variations of differences in strain sensitivity for the three samples were accounted for the variance of FBG sensor location during loading and maybe slight bending of FBG sensors existed during samples manufacturing. During the loading interval of 2 minutes, Sample L1 and Sample L2 showed noticeable increases in wavelength, which may be induced by the inelasticity of epoxy coatings. Longer time interval may be needed for stable loading/unloading strains. Since this study focuses on the interaction between loading and corrosion, these temporal fluctuations would not impact the analysis results. Fig. 11 will be used as control test results to compare with the combined loading-corrosion tests.

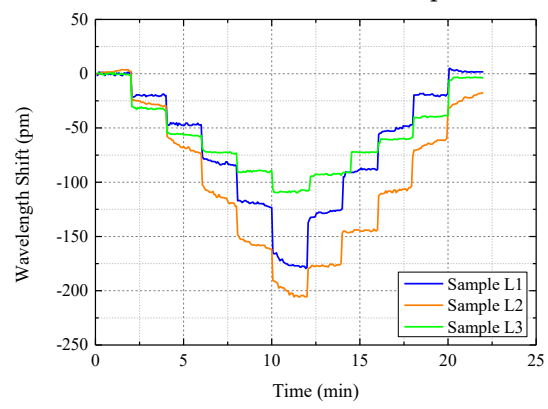


Fig. 11 Results of the Bragg wavelength shifts of the samples in the loading and unloading tests.

## 4.2. Corrosion-only tests

Fig. 12 shows the wavelength changes obtained from the corrosion-only tests. With the recorded Bragg wavelength changes, the corrosion rate of each sample can be estimated using [26]:

$$CR = \gamma \cdot \frac{d\Delta\lambda}{dt} \tag{14}$$

where,  $\gamma$  is the sensitivity of the sensor to the rate of metal corrosion. Based on Eq. (14), Table 4 lists the estimated corrosion rate of each sample. The corrosion rate of the three

epoxy-coated steel plate samples with prefabricated crack ranging from 0.28 to 1.13  $\mu\text{m/year}$ .

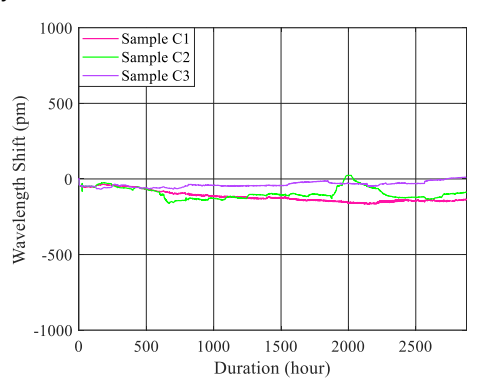


Fig. 12 Experimental results from corrosion-only tests.

Table 4 Corrosion rates of three samples.

T T T T T T T T T T T T T T T T T T T		
Sample No.	Corrosion rate for corrosion-only conditions	
	(μm/year)	
C1	1.13	
C2	0.52	
C3	0.28	

## 4.3. Combined loading-corrosion tests

Fig. 13 shows the monitored Bragg wavelength shifts of the three tested samples during the entire combined loading-corrosion tests including the gradual changes caused by corrosion and the sudden changes induced by the loading and unloading cycles. Figs. 14(a, b, c) show the visual inspection of the three tested samples at the end of the combined loading-corrosion tests. From Fig. 13, it can be seen that the changing trends of B1 and B3 were basically the same with similar wavelength shifts, indicating that they had experienced similar extent of corrosion. However, B2 showed a different trend. This different trend of B2 was because the rod to holding the weights for static loading was accidental tipped over during the 1st loading cycle. This accident may have caused premature delamination between the epoxy and the substrate, which may accelerate the development of corrosion and made the corrosion more serious than B1 and B3, which has been illustrated in Fig. 14(b) that the epoxy coating of B2 had delaminated and a large amount of brownred corrosion products were generated at end of the test. With the premature delamination, sudden significant amount of wavelength increases was noticed during and after the 6th and the 13th loading cycles, indicating that the loading may have further induced cracks which accelerated corrosion. At around 2000 hours, the corrosion rate (CR) of B2 was estimated to be 39.04 µm/year according to Eq. (14), which is close to the corrosion rate of 39.26 µm/year for bare A36 structural steel with corrosion cracks from the previous Tafel test [26]. It indicated that the steel under the epoxy coating had been severely corroded with the existences of cracks.

349 350

351

352 353

354

369

370

371

372

373

374

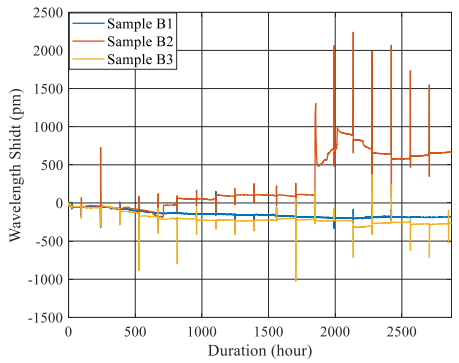


Fig. 13 Wavelength shifts of the three tested samples under combined loading-corrosion tests.

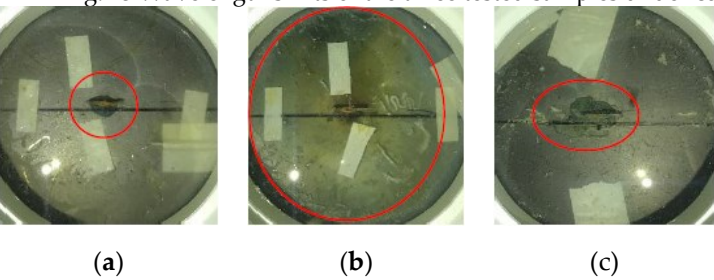
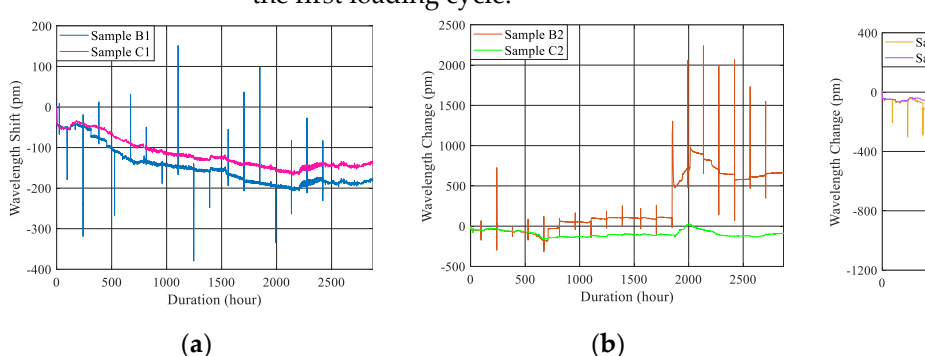


Fig. 14 Visual inspections of the three tested samples under combined loading-corrosion tests at the end of the experiments: (a) B1, (b) B2, and (c) B3.

Fig. 15 compares the Bragg wavelength shifts of the three tested samples under corrosion-only and under combined loading-corrosion tests and Table 4 compares the average corrosion rate of the corresponding tested samples under these two testing conditions. The results show that external temporary load had promoted corrosion significantly compared to corrosion-only condition. Specifically, Fig. 15 and Table 5 indicate that depending on the condition of the epoxy coating, if delamination exists in the coating, external temporary load can induce severe corrosion up to 12 times higher at the end compared to no external loads and the interactive damages induced by interaction between corrosion and loads can occur in a relatively short period of time within one week (168 hours) after the first loading cycle.



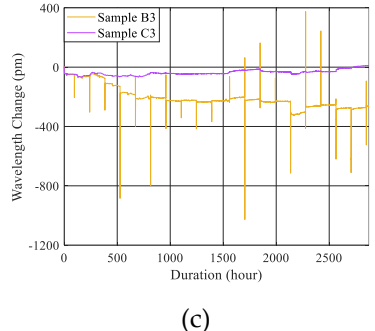


Fig. 15 Comparison of recorded Bragg wavelength changes between corrosion-only and combined loading-corrosion tests: (a) B1 versus C1, (b) B2 versus C2, and (b) B3 versus C3.

Table 5 Measured average corrosion rates of the tested samples.

Samples	Corrosion-only average corrosion rate	corrosion average	Percentage of corrosion rate increase (%)
μm/year)	corrosion rate (µm/year)		
1	1.13	1.63	44.3%
2	0.52	6.80	1207.7%
3	0.28	1.72	514.3%

5. Discussions

## 5.1. Corrosion depth severity ratio

To investigate the influence of external temporary loading on the corrosion severity, based on the corrosion depth, d, as in Eq. (5), in this paper, a corrosion depth severity ratio ( $R_d$ ) is defined as:

$$R_d = d_0/d_1 \tag{15}$$

in which,  $d_0$  is the depth of corrosion with corrosion only and  $d_1$  is the depth of corrosion with combined corrosion with external temporary loading cycles. With an expectation that external loads would increase corrosion depth, the corrosion severity ratio is expected to be smaller than 1 and a smaller corrosion depth severity ratio indicates higher impact of external temporary loading cycles on the corrosion progressing.

Figs. 16(a, b, c) show the estimated corrosion depths,  $d_0$  and  $d_1$ , and Fig. 16 (d) illustrates the corrosion depth severity ratio,  $R_d$ , for all the three tested samples. It is noted that for all three samples, the external temporary loading cycles had significantly increased the corrosion depths for all three tested samples. Clear abrupt changes in Fig. 16 (b) after Loading No. 5, 14, and 15 indicate that significant and sudden development of pitting corrosion occurred after these loading cycles. Fig. 16(d) clearly indicates that after three loading cycles, all three samples had promoted corrosion severity compared to before three loading cycles. The corrosion severity can approach to zero if coating delamination exists. In addition, since C1-B1 and C2-B2 had showed delamination in the epoxy coating, loading had a more pronounced effect on the corrosion development at the beginning of corrosion.

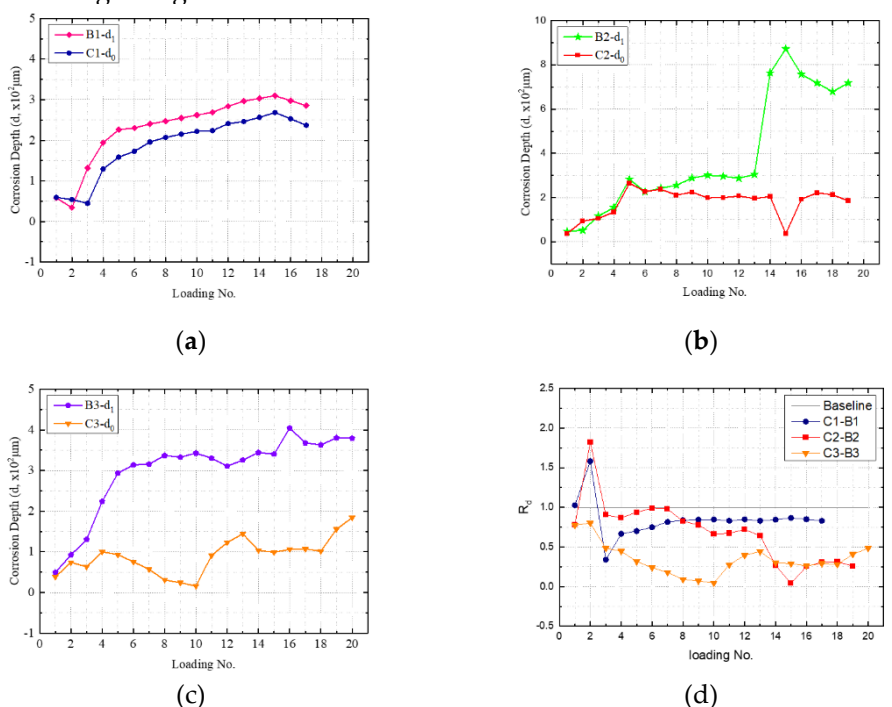


Fig. 16 Comparison corrosion depth severity ratio: (a) Sample B1-C1, (b) Sample B2-C2, (c) Sample B3-C3, and (d) Corrosion depth severity with impact from external temporary loads.

# 5.2. Corrosion width severity ratio

According to Eq. (13) and the monitored Bragg wavelength changes in Fig. (15), Figs. 17(a, b, c) show the changes of corrosion width severity ratio, which is defined as dividing the actual corrosion width ( $w_c$ ) by the initial assumed corrosion width ( $L_0$ ), under the combined loading-corrosion tests of the three tested samples with five different loading levels. As the original width of corrosion is unknown, in this study, the original width of the

424

425

426

427

428

429

430

431

432

433

434

435

436

437

438

439

440

441

442

443

444

445

446

447

448

449

450

451

453

455

456

457

458

459

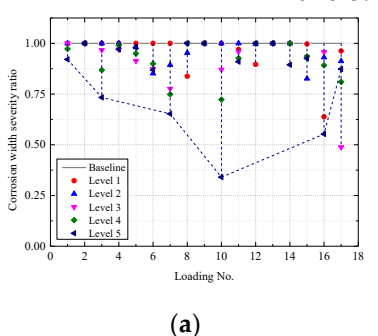
460

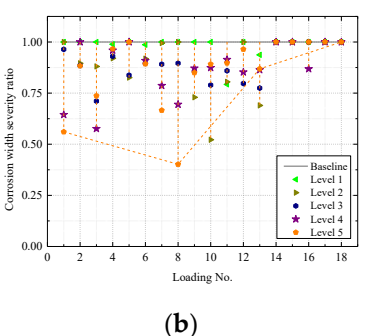
461

462

463

corrosion ( $L_0$ ) is assumed to be the diameter of the external load which equals to 0.75 in. (diameter of the loading rod) in this experiment. As the actual corrosion width usually is less than the diameter of the external load (0.75 in.), the corrosion width severity is expected to be a value of less than 1.0. The accumulation of corrosion products under FBG sensors induce an upward lift leading to the increase of the corrosion width, and as the corrosion grows more severer, the length the corrosion width is expected to be comparable and even larger than the external load diameter. Thus, the corrosion width ratio is expected to increase back to 1.0 or higher as the corrosion continuously grows. From Figs. 17(a-c), it can be seen that the envelopes of the corrosion width ratio (marked with dashed lines) after five-level loading of the three samples all decreased first and then increased, which validated the assumptions mentioned above. Among the three samples, the corrosion width ratio of B2 was restored to be 1.0, indicating that the corrosion width of B2 grew to be equal or larger than the diameter of the external load (0.75 in.) at the end of the experiment. In addition, because of the compacting effect of external loads on the corrosion products, most of the contact length also reduced first and then increased again during each loading test from level 1 to level 5. Overall, by comparing the corrosion width ratio of different samples after all the loading tests, it was found that B2 has the largest corrosion width followed by B1 and B3, which is consistent with the findings in Sections 4 and 5.1.





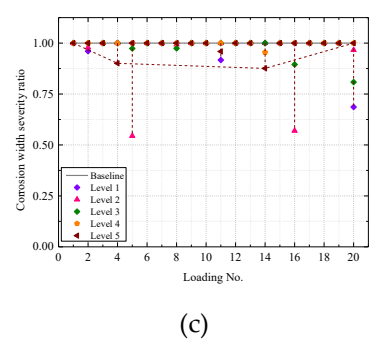


Fig. 17 Changes of corrosion width severity ratio ( $W_c/L_0$ ) under the combined loading-corrosion tests: (a) Sample B1, (b) Sample B2, and (c) Sample B3.

6. Conclusions

Experimental results proved that the FBG sensors were able to accurately monitor corrosion and the significant interactions between corrosion and external loads in real time. The most remarkable findings in this paper are listed below:

- The wavelength changes among different samples were compared. It was found that delamination of the epoxy coating would significantly accelerate corrosion in epoxy coated steel and increase the contribution of external loads on impacting corrosion.
- The comparison between the wavelength changes under corrosion-only and combined loading-corrosion tests and the corrosion depth analysis indicated that temporary external loading can significantly accelerate corrosion up to 12 times compared to no external loading, especially in the condition when the coating was delaminated.
- With combined external temporary loading and corrosion, the corrosion width ratio
  first decreased and then increased indicating a more sever corrosion, which was induced by the expansion of corrosion products and the compacting of loose corrosion
  products under external loading.

The current studies were conducted in laboratory environments which may limited the effects of loading on corrosion. In the future, further study will be performed to assess the long-term interaction of corrosion and static loads in practical applications.

**Author Contributions:** Conceptualization, L.X. and Y.H.; methodology, L.X. and Y.H.; software, L.X., S.H. and H.P.; investigation, L.X. and Y.H.; writing—original draft preparation, L.X.; writing—review and editing, Y.H., Y.B. and D.Z.; supervision, Y.H.; project

administration, Y.H.; funding acquisition, Y.H. All authors have read and agreed to the published version of the manuscript.

Funding: This research was partially funded by the National Science Foundation [grant number CMMI-1750316] and Pipeline and Hazardous Materials Safety Administration (PHMSA) of U.S. Department of Transportation [grant number 693JK31950008CAAP].

**Informed Consent Statement:** Informed consent was obtained from all subjects involved in the study.

Data Availability Statement: Not applicable.

**Acknowledgments:** The findings and opinions expressed in this article are those of the authors only and do not necessarily reflect the views of the sponsors.

**Conflicts of Interest:** The authors declare no conflict of interest.

#### References

- Popoola, L. T., Grema, A. S., Latinwo, G. K., Gutti, B. & Balogun, A. S. Corrosion problems during oil and gas production and its mitigation. International Journal of Industrial Chemistry 4, 35 (2013).
- Li, H.-N., Li, D.-S. & Song, G.-B. Recent applications of fiber optic sensors to health monitoring in civil engineering. Engineering structures 26, 1647-1657 (2004).
- 3. Lu, H., Zhang, S., Li, W., Cui, Y. & Yang, T. Synthesis of graphene oxide-based sulfonated oligoanilines coatings for synergistically enhanced corrosion protection in 3.5% NaCl solution. ACS applied materials & interfaces 9, 4034-4043 (2017).
- 4. Mahvash, F. et al. Corrosion resistance of monolayer hexagonal boron nitride on copper. Scientific Reports 7, 42139 (2017).
- 5. Vaysburd, A. & Emmons, P. How to make today's repairs durable for tomorrow—corrosion protection in concrete repair. Construction and building materials 14, 189-197 (2000).
- Fedrizzi, L., Azzolini, F. & Bonora, P. L. The use of migrating corrosion inhibitors to repair motorways' concrete structures contaminated by chlorides. Cement and Concrete Research 35, 551-561 (2005).
- 7. Nmai, C. K. Multi-functional organic corrosion inhibitor. Cement and Concrete Composites 26, 199-207 (2004).
- Vaysburd, A. M. & Emmons, P. H. Corrosion inhibitors and other protective systems in concrete repair: concepts or misconcepts. Cement and Concrete Composites 26, 255-263 (2004).
- Venkatesan, P., Palaniswamy, N. & Rajagopal, K. Corrosion performance of coated reinforcing bars embedded in concrete and exposed to natural marine environment. Progress in Organic Coatings 56, 8-12 (2006).
- 10. Talo, A., Passiniemi, P., Forsen, O. & Yläsaari, S. Polyaniline/epoxy coatings with good anti-corrosion properties. Synthetic Metals 85, 1333-1334 (1997).
- 11. Talo, A., Forsen, O. & Yläsaari, S. Corrosion protective polyaniline epoxy blend coatings on mild steel. Synthetic Metals 102, 1394-1395 (1999).
- 12. Zhou, F. L., Gong, R. H. & Porat, I. Mass production of nanofibre assemblies by electrostatic spinning. Polymer International 58, 331-342 (2009).
- 13. Akinyemi, O., Nwaokocha, C. & Adesanya, A. Evaluation of corrosion cost of crude oil processing industry. Journal of Engineering Science and Technology 7, 517-528 (2012).
- 14. Zhang, N., Chen, W., Zheng, X., Hu, W. & Gao, M. Optical sensor for steel corrosion monitoring based on etched fiber Bragg grating sputtered with iron film. IEEE Sensors Journal 15, 3551-3556 (2015).
- 15. Carpinteri, A., Lacidogna, G. & Niccolini, G. Damage analysis of reinforced concrete buildings by the acoustic emission technique. Structural Control and Health Monitoring 18, 660-673 (2011).
- 16. Zaki, A., Chai, H. K., Aggelis, D. G. & Alver, N. Non-destructive evaluation for corrosion monitoring in concrete: A review and capability of acoustic emission technique. Sensors 15, 19069-19101 (2015).
- 17. Tan, C., Shee, Y., Yap, B. & Adikan, F. M. Fiber Bragg grating based sensing system: Early corrosion detection for structural health monitoring. Sensors and Actuators A: Physical 246, 123-128 (2016).
- 18. Sun, T. et al. Novel fibre optic sensors for monitoring corrosion-related properties of concrete. (2006).
- 19. Abbasnia, R. & Farsaei, A. Corrosion detection of reinforced concrete beams with wavelet analysis. International Journal of Civil Engineering 11, 160-169 (2013).
- Surre, F., Sun, T. & Grattan, K. T. Fiber optic strain monitoring for long-term evaluation of a concrete footbridge under extended test conditionss. IEEE Sensors Journal 13, 1036-1043 (2012).

465 466

467 468 469

470 471

472

473

475

476

477 478

479

480

481

482

483

484

485

486

487 488

489

490 491

492

493 494

495

496 497

498

499

500

501

502 503

504 505

> 506 507

508 509

510

511 512

- 21. Maalej, M., Ahmed, S., Kuang, K. & Paramasivam, P. Fiber optic sensing for monitoring corrosion-induced damage. Structural Health Monitoring 3, 165-176 (2004).
- 22. López-Higuera, J. M., Cobo, L. R., Incera, A. Q. & Cobo, A. Fiber optic sensors in structural health monitoring. Journal of lightwave technology 29, 587-608 (2011).
- 23. Abdel-Jaber, H. & Glisic, B. Monitoring of long-term prestress losses in prestressed concrete structures using fiber optic sensors. Structural Health Monitoring 18, 254-269 (2019).
- 24. Majumder, M., Gangopadhyay, T. K., Chakraborty, A. K., Dasgupta, K. & Bhattacharya, D. K. Fibre Bragg gratings in structural health monitoring—Present status and applications. Sensors and Actuators A: Physical 147, 150-164 (2008).
- 25. Huang, Y. et al. Steel bar corrosion monitoring with long-period fiber grating sensors coated with nano iron/silica particles and polyurethane. Structural Health Monitoring 14, 178-189 (2015).
- 26. Deng, F., Huang, Y., Azarmi, F. & Wang, Y. Pitted corrosion detection of thermal sprayed metallic coatings using fiber Bragg grating sensors. Coatings 7, 35 (2017).
- 27. Deng, F., Huang, Y. & Azarmi, F. Corrosion behavior evaluation of coated steel using fiber Bragg grating sensors. Coatings 9, 55 (2019).
- 28. Jin, Z., Zhao, X., Zhao, T. & Yang, L. Interaction between compressive load and corrosive-ion attack on reinforced concrete with accelerated potentiostatic corrosion. Construction and Building Materials 113, 805-814 (2016).
- 29. Hariche, L., Ballim, Y., Bouhicha, M. & Kenai, S. Effects of reinforcement configuration and sustained load on the behaviour of reinforced concrete beams affected by reinforcing steel corrosion. Cement and Concrete Composites 34, 1202-1209 (2012).
- 30. Fang, C., Gylltoft, K., Lundgren, K. & Plos, M. Effect of corrosion on bond in reinforced concrete under cyclic loading. Cement and Concrete Research 36, 548-555 (2006).
- 31. Feng, X., Lu, X., Zuo, Y., Zhuang, N. & Chen, D. Electrochemical study the corrosion behaviour of carbon steel in mortars under compressive and tensile stresses. Corrosion Science 103, 66-74 (2016).
- 32. Aveldaño, R. R. & Ortega, N. F. Behavior of concrete elements subjected to corrosion in their compressed or tensed reinforcement. Construction and Building Materials 38, 822-828 (2013).
- 33. Ghosh, C., Alfred, Q. M. & Ghosh, B. Spectral characteristics of uniform fiber Bragg grating with different grating length and refractive index variation. International Journal of Innovative Research in Computer and Communication Engineering 3, 456-462 (2015).
- 34. Khan, I. & Ahmed, I. Sensing principle analysis of FBG based sensors. IOSR Journal of Electrical and Electronics Engineering (IOSRJEEE), ISSN, 2278-1676 (2012).
- 35. Huang, J. et al. Real-time monitoring for the CFRP/aluminium-alloy bonding structure during curing process using encapsulated fiber Bragg grating sensor. Optical Fiber Technology 57, 102216 (2020).
- 36. Mahjoubi, S., Tan, X. & Bao, Y. Inverse analysis of strain distributions sensed by distributed fiber optic sensors subject to strain transfer. Mechanical Systems and Signal Processing 166, 108474 (2022).
- 37. Tan, X., Bao, Y., Zhang, Q., Nassif, H. & Chen, G. Strain transfer effect in distributed fiber optic sensors under an arbitrary field. Automation in Construction 124, 103597 (2021).
- 38. Huang, Y., Bao, Y., Chen, G. & Zhou, Z. A constrained cylinder model of strain transfer for packaged fiber Bragg grating sensors embedded in inelastic medium. Structural Control and Health Monitoring 26, e2335 (2019).
- 39. Lu, S.-w. & Xie, H.-q. Strengthen and real-time monitoring of RC beam using "intelligent" CFRP with embedded FBG sensors. Construction and Building Materials 21, 1839-1845 (2007).
- 40. Miguel, J., Guilemany, J., Mellor, B. & Xu, Y. Acoustic emission study on WC–Co thermal sprayed coatings. Materials Science and Engineering: A 352, 55-63 (2003).
- 41. Popov, B. N. Corrosion engineering: principles and solved problems. (Elsevier, 2015).
- 42. Poursaee, A. in Corrosion of steel in concrete structures 19-33 (Elsevier, 2016).
- 43. Rosa, G., Oltra, R. & Nadal, M.-H. Evaluation of the coating–substrate adhesion by laser-ultrasonics: Modeling and experiments. Journal of applied physics 91, 6744-6753 (2002).
- 44. Sargent, J. Corrosion detection in welds and heat-affected zones using ultrasonic Lamb waves. Insight-Non-Destructive Testing and Condition Monitoring 48, 160-167 (2006).
- 45. Wang, G. et al. Testing of acoustic emission technology to detect cracks and corrosion in the marine environment. Journal of Ship Production and Design 26, 106-110 (2010).
- 46. Zhu, W., Rose, J., Barshinger, J. & Agarwala, V. Ultrasonic guided wave NDT for hidden corrosion detection. Journal of Research in Nondestructive Evaluation 10, 205-225 (1998).
- 47. Huang, Y., Deng, F., Xu, L. & Azarmi, F. Two-dimensional pitted corrosion localization on coated steel based on fiber Bragg grating sensors. Journal of Civil Structural Health Monitoring 10, 927-945 (2020).
- 48. Wang, M., Wang, J. & Hu, W. Preparation and corrosion behavior of Cu-8-HQ@ HNTs/epoxy coating. Progress in Organic Coatings 139, 105434 (2020).